Second harmonic scattering reveals different orientational orders inside the hydrophobic cavity of hybrid nanotubes

Ali Dhaini, Bénédicte Prelot, Antoine Thill, Gaelle Martin-Gassin, Pierre-Marie Gassin

Second Harmonic Scattering reveals different orientational orders inside the hydrophobic cavity of hybrid nanotubes

Ali DHAINI [a], Bénédicte PRELOT [a], Antoine THILL [b], Gaelle MARTIN-GASSIN [a] , Pierre-Marie GASSIN* [a]

a ICGM, Univ. Montpellier, ENSCM, CNRS, Montpellier, France.
b LIONS, NIMBE, CEA, CNRS, Université Paris-Saclay, Gif sur Yvette, France.

Corresponding author : pierre-marie.gassin@enscm.fr

Abstract :

Second Harmonic Scattering (SHS) is a suitable technique to investigate the orientational correlations between molecules. This article explores the organization of different dye molecules adsorbed within the hydrophobic porosity of hybrid organic-inorganic nanotube. Experimental polarization resolved SHS measurements highlight different orientational orders ranking from highly ordered and rigid organizations to disordered assemblies. Microscopic models of assemblies inside the pores are presented and discussed in the context of orientational correlation between the dye molecules. This work shows that the degree of order in the nanotube cavity follows the molecule's affinity within the porosity.

I. INTRODUCTION

Second Harmonic Light Scattering (SHS), a process in which two photons at the fundamental frequency are converted into one at the double frequency, is widely used to investigate colloidal aqueous interfaces[1-4] including water droplets[5, 6], and biological membranes[7, 8]. The contribution of orientational correlations in SHS intensities has been known for decades[9] and has recently found renewed interest to probe the molecular structure of various system such as liquid solution[10-13], supramolecular assembly[14], or dye inclusion

inside porous material[15]. More precisely, the SHS intensity of N emitters can be linked to the orientational correlation function $g(\boldsymbol{q}, \boldsymbol{\Omega_1}, \boldsymbol{\Omega_2})$ by the formula[12] :

$$I = G \sum_{i,j}^{N} \beta(\boldsymbol{\Omega_i})\beta(\boldsymbol{\Omega_j}) e^{i\boldsymbol{q}.(\boldsymbol{r}_i - \boldsymbol{r}_j)} =$$
$$GN[\int \beta^2(\boldsymbol{\Omega_1}) d\boldsymbol{\Omega_1} + (N-1) \iint \beta(\Omega_1)\beta(\Omega_2) g(\boldsymbol{q}, \boldsymbol{\Omega_1}, \boldsymbol{\Omega_2}) \mathrm{d}\boldsymbol{\Omega_1} \mathrm{d}\boldsymbol{\Omega_2}]$$
(1)

With G a general constant, $\mathbf{q}$ is the scattered wave vector equal to $(2\boldsymbol{k_\omega} - \boldsymbol{k_{2\omega}})$, β is the hyperpolarizability tensor expressed in the laboratory frame which depends on the orientation $\boldsymbol{\Omega_i} = (\varphi_i, \theta_i, \psi_i)$ of the molecule i. One recognizes in the equation (1) the usual separation into incoherent and coherent contributions. In bulk liquids, the coherent term which describes the interferences between the waves scattered by two molecules, would average to zero if the instantaneous relative orientation of the two molecules were completely random. On the contrary, this term would become predominant if the molecules were highly correlated and if they kept a constant relative orientation when interacting with the light pulse. This condition can be realized when molecules are adsorbed onto a colloidal system or confined inside a porous material[16]. The strength of the different interactions, molecule-material, molecule-solvent and molecule-molecule is the key point that drives this condition.

Methylated imogolite (IMO-CH_3) is an hybrid material[17] formed by a single wall aluminosilicate clay nanotube displaying methyl moiety in the inner surface, making its cavity hydrophobic, while the external nanotube surface is hydrophilic due to hydroxyl groups. This material forms stable dispersion of monodisperse single digit hydrophobic nanopores (diameter ~1.8 nm) in water and has demonstrated its ability to encapsulate organic molecules[18-20] thanks to the hydrophobic effect which pushes hydrophobic molecules inside the hydrophobic cavity. This material exhibits promising applications in environmental remediation such as dye and pollutant degradation[21], and fuel production[22, 23]. Among the numerous questions about the mechanisms involved in such treatments, the orientation and the long range organization of molecules inside the nanotube is crucial to rationalize and better understand the microscopic steps that drive the chemical reactions[24]. In a recent work[20], it was demonstrated that an azoic dye can be adsorbed inside this cavity, and that Polarization Resolved SHS (PR-SHS) is able to probe its organization. The present study is extended to other dyes adsorbed inside the nanotube and different organization are highlighted. The PR-SHS evolution along the adsorption isotherm is used to disentangle the coherent and incoherent contribution in the whole SHS signal and thus to extract insights

about the orientational order of the dye within the nanotube. Three different dye molecules are studied here, with different shapes, charges, and affinity with the nanotube. The manuscript is divided in two parts. First, the SHS response of free solvated molecules are presented. These experiments are refereed in the following as Hyper Rayleigh Scattering (HRS) experiment as the SHS intensity is mainly driven by the incoherent term of equation 1. From these experiments the hyperpolarizability tensor of each dye molecule can be evaluated. The second part presents results when IMO-CH_3 nanotubes are added to the solution. Different models considering different orientational orders for the supramolecular dye assemblies within the pores are presented and discussed in regards to the experimental results.

II. THEORETICAL BACKGROUND OF PR-SHS

In the case of a solution containing free solvated dye, the PR-SHS signal is refereed as PR-HRS. This light can be written as the sum of two contributions, the solvent and the solute:

$$I^{\Gamma}_{HRS,solution}(\gamma) = I^{\Gamma}_{HRS,dye}(\gamma) + I^{\Gamma}_{HRS,solvent}(\gamma) \quad (2)$$

The angles γ and Γ are respectively the incident polarization angle and the output polarization state, (Γ = V) for vertically and (Γ = H) for horizontally output state, as depicted on Figure 1A. The solvent contribution can be written as[12]:

$$I^{\Gamma}_{HRS,solvent}(\gamma) = K \times C_s\left\{a^{\Gamma}_{solvent}\cos^4(\gamma) + b^{\Gamma}_{solvent}\cos^2(\gamma)\sin^2(\gamma) + c^{\Gamma}_{solvent}\sin^4(\gamma)\right\} \quad (3)$$

where K is a constant prefactor including experimental parameters, C_s is the solvent concentration, C_s=55.56 mol/L for water, and the $a_{solvent}$, $b_{solvent}$, $c_{solvent}$ coefficients depends on the hyperpolarizability components β_{ijk} of the solvent molecules and eventually on the orientational correlation function if the solvent exhibits long range correlation[12]. The dye contribution can also be written with the same formalism as:

$$I^{\Gamma}_{HRS,dye}(\gamma, C_{dye}) =$$
$$K \times C_{dye}\left\{a^{\Gamma}_{HRS,dye}\cos^4(\gamma) + b^{\Gamma}_{HRS,dye}\cos^2(\gamma)\sin^2(\gamma) + c^{\Gamma}_{HRS,dye}\sin^4(\gamma)\right\} \quad (4)$$

with K is the same constant as in equation (2). The $a_{HRS,dye}$,$b_{HRS,dye}$ and $c_{HRS,dye}$ coefficients are here totally determined by the hyperpolarizability components β_{ijk} of the dye molecules as the dye are well dispersed and solvated in the solvent.

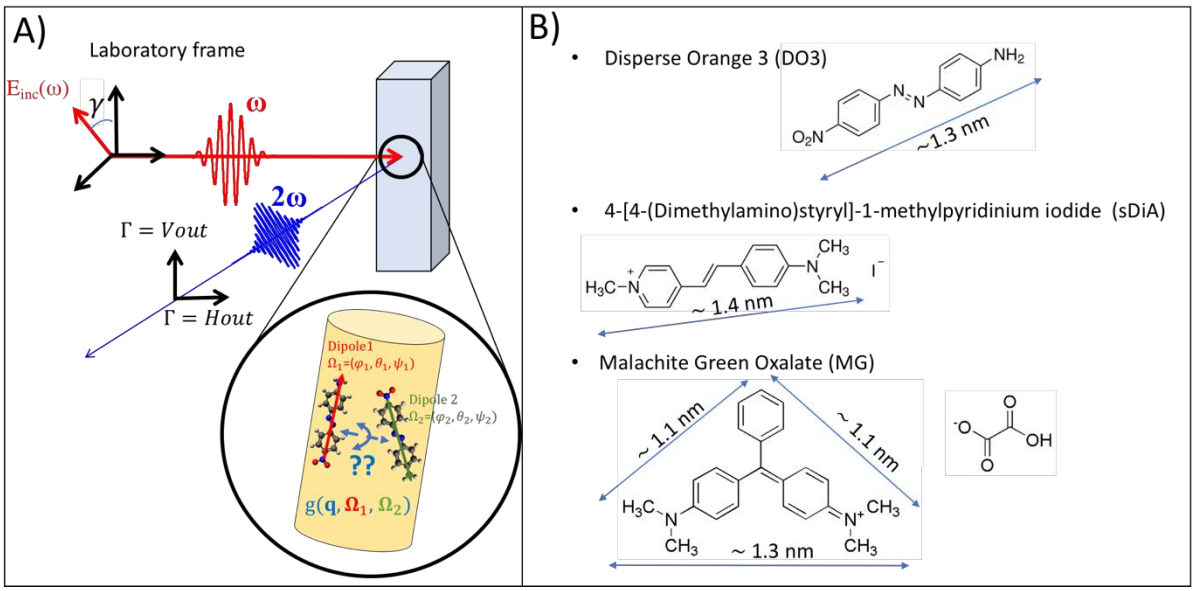

Figure 1. A) The experimental setup with the input polarization angle (γ) and output polarization angle Γ, with V for Vertical and H for Horizontal polarization state. B) The three dyes molecules studied here are labeled in the following as DO3, sDiA and MG. Their dimensions are given for the discussion.

When colloidal IMO-CH_3 nanotubes are added in the solution, the SHS signal becomes in this case a sum of tree contributions: the solvent contribution, the free dye in solution contribution and the adsorbed dye contribution. The nanotube contribution is negligible as it is justified in the Supporting Information. The whole SHS intensity of the sample is written as:

$$I^{\Gamma}_{SHS,sample}(\gamma, C_{dye}, C_{NT}) = I^{\Gamma}_{SHS,adsorbed\ dye}(\gamma, Q, C_{NT}) + I^{\Gamma}_{HRS,dye}(\gamma, Ce) + I^{\Gamma}_{HRS,solvent}(\gamma) \quad (5)$$

Here $I_{HRS,solvent}$ is the solvent contribution in the presence of imogolite nanotube. This term is slightly different than the pure water contribution as it can be seen in the Figure S5 in the SI. Here C_{dye} is the total concentration of dye in the system, Q is the amount of dye adsorbed inside the nanotube, expressed in mol/g, and C_e is the concentration of free dye in solution,

expressed in mol/L. The relationship between Q and C_e is called the adsorption isotherm and will be presented and determined for each dye in the following. C_{NT} is the mass concentration of nanotube in the solution expressed in g/L and is connected to Q and C_e by the mass conservation equation:

$$C_{dye} = C_e + Q \times C_{NT} \quad (6)$$

The adsorbed dye contribution can also be expressed as:

$$I^{\Gamma}_{SHS,adsorbed\ dye}(\gamma, Q, C_{NT}) = K \times C_{NT} \times \left\{a^{\Gamma}_{SHS,dye}(Q)\cos^4(\gamma) + b^{\Gamma}_{SHS,dye}(Q)\cos^2(\gamma)\sin^2(\gamma) + c^{\Gamma}_{SHS,dye}(Q)\sin^4(\gamma)\right\} \quad (7)$$

K being the same constant as in equations 3-4. The $a_{SHS,dye}$, $b_{SHS,dye}$ and $c_{SHS,dye}$ coefficients in equation (7) depends on the amount of dye adsorbed inside the nanotube Q, the hyperpolarizability components β_{ijk} of the dye molecules, and the orientational order of the adsorbed dye as depicted by the equation (1). In the following, different microscopic models will be presented and computed in order to calculate the value of these $a_{SHS,dye}$, $b_{SHS,dye}$ and $c_{SHS,dye}$ coefficients.

III. MATERIALS AND METHODS

A. Chemicals

The 4-(4-(dimethylamino)styryl)-1-methylpyridinium iodide (sDiA), MW=366.24 g/mol, the Malachite Green Oxalate (MG), MW =463.5 g/mol and the Disperse Orange 3 (DO3), MW=242.23 g/mol are obtained from Sigma Aldrich at a purity of respectively 98%, 95% and 96 %. Absolute ethanol is also from Sigma Aldrich. 18 MΩ.cm water (MilliQ) is used. The IMO-CH_3 nanotube synthesis is described elsewhere[20] and additional details can be found in these published protocols[17, 25, 26]. The IMO-CH_3 mass concentration, in the resulting suspension, is around 6.5 g/L and will be diluted to the adequate concentration.

B. Sample preparation

For the sDiA and MG dyes, a stock solution at 1 mM is prepared in water. From this stock solution, different samples containing the adequate dye concentrations and 0.25 g/L of IMO-CH_3 nanotubes are prepared and equilibrated during 24 h. For the hydrophobic DO3

dye, the protocol is slightly different because the DO3 dye is not soluble in water. Then, a stock solution of DO3 in ethanol at 1mM is prepared. From this stock solution, different samples containing the adequate dye concentration in ethanol are prepared, the ethanol is then evaporated at room temperature and pressure, the residue was dispersed in the 0.25g/L IMO-CH_3 aqueous solution. The solution is also equilibrated during 24 h prior to the SHS measurements.

C. PR-HRS and PR-SHS measurements

The polarization resolved SHS experimental setup is detailed elsewhere[27]. Briefly, it was based on a femtosecond laser source operating at a fundamental wavelength of 800 nm with an average power of 750 mW onto the sample. This beam was focused by a microscope objective (Ealing 10×, numerical aperture 0.25.) onto the sample at 1 mm close to the output cell window. The SHS intensity is monitored in the right-angle direction as a function of the input polarization angle γ, see Figure 1, which was selected with a rotating half-wave plate. The second harmonic light was selected in the Γ state by an analyzer placed in front of the spectrometer either in the vertical (V) or horizontal (H) state. All experimental data were recorded for 10 s under stirring conditions; a magnetic stirrer is operated in the 1 cm quartz cell measurement. All data, have been repeated independently three time and are well reproducible with a relative standard deviation never higher than 5%.

D. Adsorption isotherm measurements

For the sDiA and MG dye, the adsorption isotherms were conducted at 20°C using the depletion method in batch conditions. A series of dye having various initial concentrations ranking from 0.005 to 0.150 mM, in 0.25 g/L IMO-CH_3 suspensions, were prepared. The suspensions were shaken overnight and filtered after using 0.22 μm PTFE filters. The equilibrium concentration of dye in the supernatant Ce is determined from UV−Vis absorbance spectra (JASCO V-670). The dye concentration in the supernatant is measured at a wavelength of 449 nm for the sDiA and 620 nm for MG. For each initial dye concentration, the adsorption capacity Q is then determined by subtraction, according to the equation (6), and plot as a function of Ce. For the DO3 dye, we investigate different DO3 concentration in 0.25 g/L IMO-CH_3 suspension as described in the sample preparation section. When the total DO3 concentration is below 0.06 mM, all the dye are well solubilized and are all are

incorporated inside the nanotube. When the total DO3 concentration exceeds 0.06 mM, dyes start to precipitate in solution.

E. PR-HRS and PR-SHS modelling

In the case of purely incoherent emitters, theory of PR-HRS is well known[9, 28] and the hyperpolarizability components can be deduced from the experimental $a_{HRS,dye}$, $b_{HRS,dye}$, $c_{HRS,dye}$ coefficients. The full equations, depending on the symmetry of the molecular emitters are given in Supporting Information (SI). For the water solvent, more rigorous models[10] can be used, taking into account both coherent contribution and hyperpolarizability fluctuation. As the contribution of the solvent is not the topic of this work, the incoherent model is simply considered here.

For the case of the adsorbed dye contribution, the computational program PySHS[29, 30] has been used to compute the $a_{SHS,dye}$, $b_{SHS,dye}$, $c_{SHS,dye}$ coefficients given in equation (7) for different microscopic models of organization inside the nanotube. In all cases, a 250 nm monodisperse distribution for the nanotube length is considered in agreement with the typically average length observed by atomic force microscopy[31] (additional details are in SI). The inputs of the program are the hyperpolarizability of the dye molecules β_{dyes}, the position and orientation ($\mathbf{r}_i$, $\mathbf{\Omega_i}$) of each dye adsorbed within the nanotube, and the optical parameters like the refractive index of the solution and laser wavelength. Different kind of organizations are considered: i) organization with well-defined orientations for each molecule and on the contrary, ii) organization with less defined orientation of the molecule. In this last case, it means that the orientations are randomly distributed. In such case, for similar microscopic configurations, we observed high fluctuations in the predicted SHS Intensity, with a typical Relative Standard Deviation (RSD) of about 40%. That is why, for each calculation, statistics has been evaluated on 30 sample configurations.

IV. RESULTS AND DISCUSSION

A. HRS Results

Figure 2 presents the HRS intensity evolution as a function of the different dye concentrations and the corresponding polarization plots. Using the symmetry properties of each molecule, and an incoherent emitters model, the best molecular hyperpolarizability components are determined. All the solid lines presented in Figure 2 are obtained with the model equations (2-4) and (S7-S24) and with the hyperpolarizability tensor given in Table 1. The K constant defined in the equations (2)-(4) has been set at a fixed value equal to 0.064, in

order to get the $\beta_{zzz,water}$ equal to 1. In other words, it means that all the β components have been normalized by $\beta_{zzz,water}$value. The experimental data shows that the DO3 and sDiA molecules are 1D molecule with only the β_{zzz} not zero component as already shown in this work[32]. The MG dye, exhibits a main element, the β_{zxx} component, with a small contribution of the β_{xxz} component, in agreement with work reported in the literature[33]. Each molecular hyperpolarizability components deduced from the HRS studies presented here, will be used in the following as an input parameter for the different models.

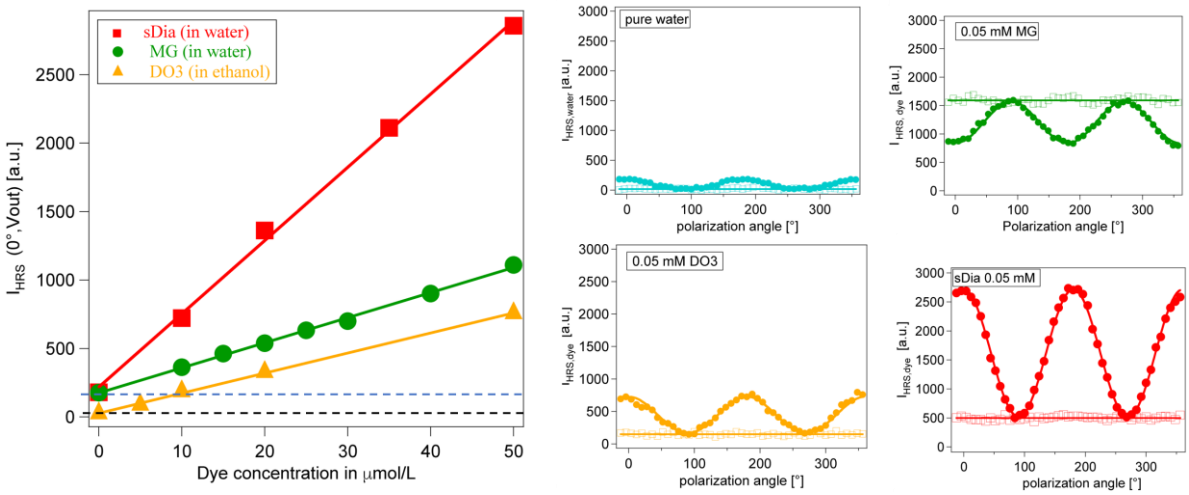

Figure 2. *Left.* HRS evolution in the (0° in, Vout) polarization state for the three different dye solutions. The MG and sDiA dyes are solvated in water whereas the DO3 is in ethanol solvent. The solid lines are obtained with the equations (2-4) and (S7-S24) with the hyperpolarizability components given in Table 1. The dashed lines are the solvent contribution in the HRS intensity: water contribution (blue) and ethanol contribution (black) *Right.* The polarization plots of the water contribution and the different dyes contribution, each dye being at 0.05 mM. The full circles are obtained in the Vout polarization configuration, and the empty square in the Hout configuration. The solid lines are the model equations (2-4) and (S7-S24) with the hyperpolarizability components given in Table 1.

Table 1. Molecular hyperpolarizability components. All the components have been normalized by the $\beta_{zzz,water}$.

Molecule	Hyperpolarizability [a. u.]

Water	$\beta_{zzz} = 1 \quad \beta_{zxx} = \beta_{xxz} = \beta_{xzx}$=0.7 $\beta_{zyy} = \beta_{yyz} = \beta_{yzy}$=0.6
DO3	$\beta_{zzz} = 4500$
sDiA	$\beta_{zzz} = 8590$
MG	$\beta_{zxx} = 9350 \qquad \beta_{xxz} = \beta_{xzx} = 935$

B. Adsorption Isotherm

Figure 3 presents the adsorption isotherm determined for the two water soluble dyes, *i.e.* sDiA and MG. The experimental data are fit with a Langmuir like model, equation (8), and the parameters are given in Table 2.

$$Q(C_e) = \frac{Q_{max} C_e}{a + C_e} \quad (8)$$

Here Q and Q_{max} are respectively the quantity adsorbed and its value at saturation, and a is the Langmuir Szyszkowski constant. The solid orange curve depicts the particular DO3 dye behavior. Indeed, for this dye, all the molecules are adsorbed inside the pore, with no dye free in solution, as long as the saturation is not reached. When the saturation is reached, the molecules are insoluble in the solution and that is represented on the Figure 3 by the dashed line. The comparison of these 3 behaviors shows that the dye's affinity for the hydrophobic cavity follows the order: DO3 > MG > sDiA.

To get a microscopic view, a model of monodispersed length nanotubes is used in the following and justified in SI. The imogolite suspension is thus modelized by system composed of 250 nm monodispersed nanotubes. Considering this model, the adsorbed quantity Q expressed in mmol/g can also be expressed as a number of dye molecules per nanotube $N_{dyes/NT}$ according to the following equation:

$$N_{dyes/NT} = Q \times N_A \times \mu_{IMO} \times l \quad (9)$$

with N_A is the Avogadro Constant, μ_{IMO} is the linear mass of IMO-CH3, μ_{IMO} =1,4.10^{-20} g/nm, and l is the length of the nanotube, *i.e.* 250 nm.

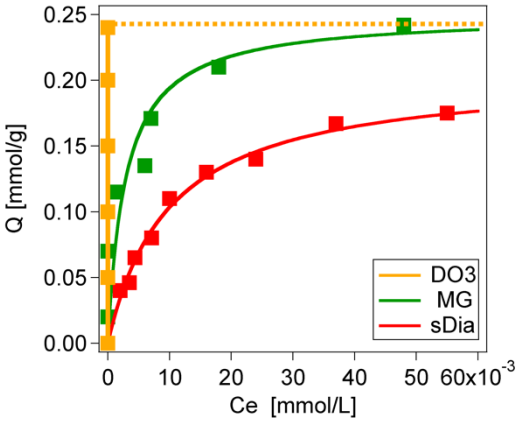

Figure 3. Adsorption isotherm for the three dyes. The colored square are the experimental data points and the solid lines are the Langmuir model, equation (8).

Table 2. Langmuir parameters obtained from the fit in Figure 3.

	Q_{max} [mmol/g]	a [mmol/l]	Q_{max} [$N_{dyes/NT}$]
DO3	0.24	0.000	506
sDia	0.19	0.010	400
MG	0.25	0.003	527

C. SHS of Dye inclusion

The Figure 4 top 1), 2) and 3) present the adsorbed dye contribution in the experimental SHS intensity as a function of the adsorbed quantity Q. To interpret these evolutions, different orientational orders depicted in Figure 4 down, are computed and compared with the experimental data. The position of each dye in the nanotube are regularly spaced and the different angles used to define the molecular orientation $\boldsymbol{\Omega}_i = (\varphi_i, \theta_i, \psi_i)$ are represented in Figure 4 down. A first set of models, models A, B, C, deals with totally correlated dyes adsorbed inside the nanotube. These models consider different orientations, radial or axial of the dye inside the nanotube. The model A and B are no-centrosymmetric organization and exhibits thus a quadratic variation with Q, see Figure 4.1) as expected for totally correlated dye. On the contrary, the model C is a centrosymmetric organization and leads thus to a zero SHS intensity, see Figure 4.1). The second set of models, models D, E, F introduces more disorder in the organization. The model D is totally disorganized, which means that the orientation of each dye is totally uncorrelated to its neighbors. To simulate that, the orientation of each dye is assigned randomly. The models F, G are a mix of order and

disorder. It means that two orientation angles, θ and ψ are fixed, and φ is randomly distributed in a more or less large interval as it is given in the Figure 4 down.

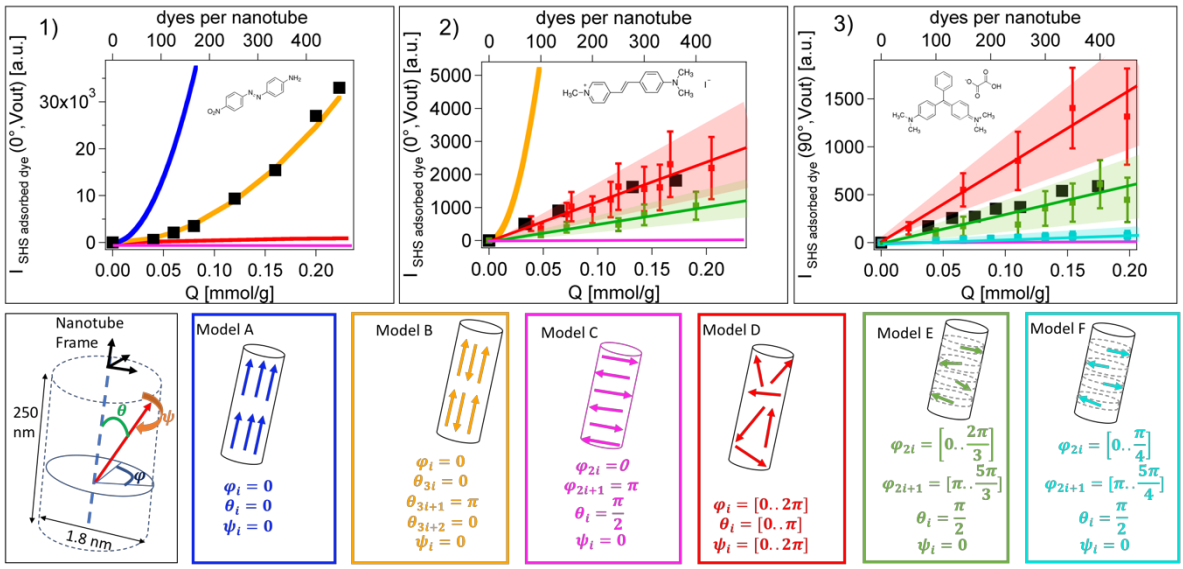

Figure 4. Up. The adsorbed dye SHS contribution as a function of the adsorbed amount quantity Q for the different dyes 1) DO3 in the [0°,V_{out}] polarization state, 2) sDiA in the [0°,V_{out}] polarization state, and 3) MG in the [90°,V_{out}] polarization state. The black square are the experimental data points. The solid colors line and the color points are the calculation given by the different models described on the bottom of the figure 4. For the models A,B,C, as the microscopic configuration is fixed, the computation is always reproducible and thus no error bars are given. This is not the case for the models D,E,F, where error bars represent the standard deviation of the computation. In that case, the solid color line is a linear regression done on these points. The colored regions are a guide for the eyes.

The variation of the DO3 SHS signal fits remarkably well with the model B (Figure 4.1), supporting the hypothesis that the DO3 dye adsorbed with trimers of tail–head molecules. These trimers probably form a chain spanning the whole nanotubes as discussed in a previous work[20] with PR-SHS measurements. The evolution presented in Figure 4.1) shows that this model is valid over all the adsorption process, and that the DO3 dyes fill as trimer the nanotube even at low density. They do not exist as monomer in the nanotube. On the contrary, the variation of the sDiA SHS signal matches with the model D domain (Figure 4.2), represented by the red area, with no correlation between the dyes. The filling of the nanotube with the sDiA dye is less compact and the average distance between sDiA dyes is larger than for the other dyes, DO3 and MG. This probably allows movements and such disorder. The

Figure 4.3 presents the variation of the MG SHS signal on a different polarization configuration (90°,Vout) because for this system, the sensitivity is better. The SHS intensity is smaller than the no correlation model D. This likely means that the MG dyes are organized in a close to centrosymmetric organization where the interferences between the second harmonic light emitted by the dye partially cancelled. The microscopic organization is thus not strictly the model C which would give zero SHS contribution. That is why two different models, E and F in Figure 4.3), that are close to a centrosymmetric organization are tested. The model F is closer to a centrosymmetric organization than the model E which is defined with a larger variation range of the φ angle. The comparison with the experimental data shows that the model E is better to reproduce them. It is difficult at this point to precisely assert how are organized the MG dyes as different microscopic configuration can lead to the same SHS intensity. Nevertheless, it is also clear that the disorder model D does not work and that a close to centrosymmetric organization is requisite to explain these data. From the shape of the MG dye and the size of the cavity, the models E and F seem probable. To summary this part, three different dye behaviors within the nanotube can be distinguished. Firstly, the DO3 dyes are adsorbed with a constant relative orientation leading to a large coherent contribution in the SHS intensity. Secondly, the sDiA dyes are adsorbed with no organization inside the nanotube leading to pure incoherent SHS intensity. Finally, the MG dyes are adsorbed with a partial order inside the nanotube leading to a weak contribution of the coherent part. As the organization may be close to a centrosymmetric assembly, the global SHS intensity is weaker than a pure incoherent contribution. It can be noticed that the trend in the organization order follows the molecule's affinity within the porosity according to: DO3>MG>sDiA.

V. CONCLUSION

This work explores the orientational order of different dye inclusion inside hybrid imogolite nanotube in the context of polarization resolved SHS. Three different dye molecules behavior inside the nanopore are analyzed. The most hydrophobic dye, the DO3 molecule, exhibits the highest affinity with the nanotube, and a dominant coherent contribution in the SHS intensity is observed. Along the possible microscopic organizations, the tail–head trimers assembly parallel to the nanotube wall, is the only configuration that can reproduce the experimental data. The second dye in term of the affinity with the material, is the MG dye. The analysis of the SHS intensity shows that this dye adsorbed inside the nanotube with a not negligible coherent contribution in the SHS intensity. Considering the

space available within the nanotube, this contribution is attributed to a radial organization, *i.e.* with a θ angle around 90°, and with degrees of freedom for the φ angle. The last system, the sDiA dyes, show less affinity with the nanotube and exhibits no coherent contribution in the SHS intensity. This is attributed to a more disorder organization inside the nanotube. Our study provides a systematic investigation of the dye correlation inside porous material, the influence of the order/disorder incidence onto the PR-SHS signal and offers practical methodology to test different microscopic organization. One perspective of this work would be to validate the approach developed here by a direct comparison with molecular dynamics trajectory.

SUPPLEMENTARY MATERIAL

See the supplementary material for : 1) Theory and equations used in the calculation ; 2) PySHS calculation : a step by step example ; 3) Comparison between the PySHS calculation versus an analytical model ; 4) Effect of the nanotube length on the SHS Intensity ; 5) Additional experimental data 6) AFM Information about the length of the nanotube

ACKNOWLEDGMENTS

The authors thank the ANR BENALOR for funding (ANR-20-CE09-0029). The authors thank also Dr. Pierre Picot, Fadwa Alfadel Raad, Dr. Naseem Ramsahye, Prof. Jerzy Zajac and Prof. Philippe Trens for fruitful discussions about hybrid imogolite materials.

AUTHOR DECLARATIONS

Conflict of Interest

The authors have no conflicts to disclose.

Author Contributions

PMG, GMG, BP and AT conceived and designed the work. AD and GMG performed the SHS experiments and PMG carried out the theoretical calculations. All authors discussed the results and contributed to the manuscript.

AD: Formal analysis (lead); Investigation (lead); Validation (lead); Visualization (lead);

BP : Conceptualization (equal); Funding acquisition (lead); Project administration (lead); Supervision (supporting);

AT: Conceptualization (lead); Funding acquisition (lead)

GMG: Formal analysis (lead); Investigation (lead) Conceptualization (lead); Funding acquisition (lead); Supervision (lead); Writing – review & editing (supporting).

PMG: Investigation (lead); Validation (lead); Visualization (lead); Conceptualization (equal); Formal analysis (supporting); Writing – original draft (lead); Writing – review & editing (lead).

DATA AVAILABILITY

The data that support the findings of this study are available from the corresponding author upon reasonable request.

REFERENCES

1. G. Gonella and H.-L. Dai, *Langmuir*, 2014, **30**, 2588-2599.
2. K. B. Eisenthal, *Chemical Reviews*, 2006, **106**, 1462-1477.
3. H. Wang, E. C. Y. Yan, E. Borguet and K. B. Eisenthal, *Chemical Physics Letters*, 1996, **259**, 15-20.
4. G. Gonella, C. Lütgebaucks, A. G. F. de Beer and S. Roke, *The Journal of Physical Chemistry C*, 2016, **120**, 9165-9173.
5. N. Smolentsev, Y. Chen, K. C. Jena, M. A. Brown and S. Roke, *The Journal of Chemical Physics*, 2014, **141**.
6. S. Roke and G. Gonella, *Annual Review of Physical Chemistry*, 2012, **63**, 353-378.
7. M. Sharifian Gh, M. J. Wilhelm and H.-L. Dai, *The Journal of Physical Chemistry Letters*, 2016, **7**, 3406-3411.
8. E. F. Page, M. J. Blake, G. A. Foley and T. R. Calhoun, *Chemical Physics Reviews*, 2022, **3**.
9. R. Bersohn, Y. H. Pao and H. L. Frisch, *The Journal of Chemical Physics*, 1966, **45**, 3184-3198.
10. G. Le Breton, O. Bonhomme, E. Benichou and C. Loison, *The Journal of Physical Chemistry Letters*, 2023, **14**, 4158-4163.
11. D. P. Shelton, *J Chem Phys*, 2015, **143**, 134503.
12. J. Duboisset, F. Rondepierre and P.-F. Brevet, *The Journal of Physical Chemistry Letters*, 2020, **11**, 9869-9875.
13. G. Tocci, C. Liang, D. M. Wilkins, S. Roke and M. Ceriotti, *The Journal of Physical Chemistry Letters*, 2016, **7**, 4311-4316.

14. M. Moris, M.-P. Van Den Eede, G. Koeckelberghs, O. Deschaume, C. Bartic, S. Van Cleuvenbergen, K. Clays and T. Verbiest, *Communications Chemistry*, 2019, **2**, 130.
15. P.-M. Gassin, B. Prelot, B. Grégoire and G. Martin-Gassin, *Langmuir*, 2018, **34**, 12206-12213.
16. M. Assaf, G. Martin-Gassin, B. Prelot and P.-M. Gassin, *Langmuir*, 2022, **38**, 1296-1303.
17. I. Bottero, B. Bonelli, S. E. Ashbrook, P. A. Wright, W. Zhou, M. Tagliabue, M. Armandi and E. Garrone, *Physical Chemistry Chemical Physics*, 2011, **13**, 744-750.
18. M. S. Amara, E. Paineau, S. Rouzière, B. Guiose, M.-E. M. Krapf, O. Taché, P. Launois and A. Thill, *Chemistry of Materials*, 2015, **27**, 1488-1494.
19. P. Picot, F. Gobeaux, T. Coradin and A. Thill, *Applied Clay Science*, 2019, **178**, 105133.
20. A. Dhaini, F. Alfadel Raad, A. Thill, B. Prelot, G. Martin-Gassin and P.-M. Gassin, *Physical Chemistry Chemical Physics*, 2023, **25**, 22913-22919.
21. S. Patra, D. Schaming, P. Picot, M.-C. Pignié, J.-B. Brubach, L. Sicard, S. Le Caër and A. Thill, *Environmental Science: Nano*, 2021, **8**, 2523-2541.
22. M.-C. Pignié, V. Shcherbakov, T. Charpentier, M. Moskura, C. Carteret, S. Denisov, M. Mostafavi, A. Thill and S. Le Caër, *Nanoscale*, 2021, **13**, 3092-3105.
23. E. Paineau, G. Teobaldi and P. Jiménez-Calvo, *Global Challenges*, 2024, **8**, 2300255.
24. S. Patra, F. Testard, F. Gobeaux, L. Sicard, D. Shaming, S. L. Caër and A. Thill, *Nanoscale*, 2023, **15**, 4101-4113.
25. M. Boyer, E. Paineau, M. Bacia-Verloop and A. Thill, *Applied Clay Science*, 2014, **96**, 45-49.
26. P. Picot, Y. Liao, E. Barruet, F. Gobeaux, T. Coradin and A. Thill, *Langmuir*, 2018, **34**, 13225-13234.
27. P.-M. Gassin, S. Bellini, J. Zajac and G. Martin-Gassin, *The Journal of Physical Chemistry C*, 2017, **121**, 14566-14571.
28. S. Brasselet and J. Zyss, *J. Opt. Soc. Am. B*, 1998, **15**, 257-288.
29. L. Boudjema, H. Aarrass, M. Assaf, M. Morille, G. Martin-Gassin and P.-M. Gassin, *Journal of Chemical Information and Modeling*, 2020, **60**, 5912-5917.
30. L. Boudjema, H. Aarrass, M. Assaf, M. Morille, G. Martin-Gassin and P.-M. Gassin, *Journal of Chemical Information and Modeling*, 2021, **61**, 5719-5719.
31. P. Picot, O. Taché, F. Malloggi, T. Coradin and A. Thill, *Faraday Discussions*, 2016, **191**, 391-406.
32. G. Revillod, J. Duboisset, I. Russier-Antoine, E. Benichou, G. Bachelier, C. Jonin and P.-F. Brevet, *The Journal of Physical Chemistry C*, 2008, **112**, 2716-2723.
33. V. Ostroverkhov, R. G. Petschek, K. D. Singer and R. J. Twieg, *Chemical Physics Letters*, 2001, **340**, 109-115.